The Astrophysical Journal, 854:69 (14pp), 2018 February 10 https://doi.org/10.3847/1538-4357/aaa66e
© 2018. The American Astronomical Society. All rights reserved.

Spectroscopic Observations of the Outflowing Wind in the Lensed Quasar SDSS J1001+5027*

Toru Misawa[1], Naohisa Inada[2], Masamune Oguri[3,4,5], Jane C. Charlton[6], Michael Eracleous[6,7], Suzuka Koyamada[8], and Daisuke Itoh[8]

[1] School of General Education, Shinshu University, 3-1-1 Asahi, Matsumoto, Nagano 390-8621, Japan; misawatr@shinshu-u.ac.jp
[2] Department of Physics, National Institute of Technology, Nara College, Yamatokohriyama, Nara 639-1080, Japan
[3] Research Center for the Early Universe, University of Tokyo, 7-3-1 Hongo, Bunkyo-ku, Tokyo 113-0033, Japan
[4] Department of Physics, University of Tokyo, 7-3-1 Hongo, Bunkyo-ku, Tokyo 113-0033, Japan
[5] Kavli Institute for the Physics and Mathematics of the Universe (Kavli IPMU, WPI), University of Tokyo, Chiba 277-8583, Japan
[6] Department of Astronomy and Astrophysics, The Pennsylvania State University, 525 Davey Lab, University Park, PA 16802, USA
[7] Institute for Gravitation and the Cosmos, The Pennsylvania State University, 525 Davey Lab, University Park, PA 16802, USA
[8] Department of Physics, Faculty of Science, Shinshu University, 3-1-1 Asahi, Matsumoto, Nagano 390-8621, Japan
Received 2017 September 3; revised 2017 December 21; accepted 2018 January 6; published 2018 February 13

Abstract

We performed spectroscopic observations of the small-separation lensed quasar SDSS J1001+5027, whose images have an angular separation $\theta = 2\farcs86$, and placed constraints on the physical properties of gas clouds in the vicinity of the quasar (i.e., in the outflowing wind launched from the accretion disk). The two cylinders of sight to the two lensed images go through the same region of the outflowing wind and they become fully separated with no overlap at a very large distance from the source ($\sim$330 pc). We discovered a clear difference in the profile of the C IV broad absorption line (BAL) detected in the two lensed images in two observing epochs. Because the kinematic components in the BAL profile do not vary in concert, the observed variations cannot be reproduced by a simple change of ionization state. If the variability is due to gas motion around the background source (i.e., the continuum source), the corresponding rotational velocity is $v_{\rm rot} \geqslant 18{,}000\,{\rm km\,s^{-1}}$, and their distance from the source is $r \leqslant 0.06$ pc assuming Keplerian motion. Among three Mg II and three C IV NAL systems that we detected in the spectra, only the Mg II system at $z_{\rm abs} = 0.8716$ shows a hint of variability in its Mg I profile on a rest-frame timescale of $\Delta t_{\rm rest} \leqslant 191$ days and an obvious velocity shear between the sightlines whose physical separation is $\sim$7 kpc. We interpret this as the result of motion of a cosmologically intervening absorber, perhaps located in a foreground galaxy.

Key words: quasars: absorption lines – quasars: individual (SDSS J1001+5027)

1. Introduction

AGN outflow, which could be powered by various mechanisms (e.g., radiation or magnetic pressure, and magnetocentrifugal forces), is a very important process in the evolution of quasars as well as the evolution of their host galaxies because (1) they may facilitate the extraction of angular momentum from accreting gas, allowing gas accretion to proceed (e.g., Blandford & Parne 1982; Emmering et al. 1992; Konigl & Kartje 1994; Everett 2005), (2) they provide energy and momentum feedback to the interstellar medium (ISM) of host galaxy and to the intergalactic medium (IGM), and inhibit star formation activity (e.g., Springel et al. 2005), and (3) they may enrich the IGM with heavy elements (e.g., Hamann et al. 1997a; Scannapieco & Oh 2004; Gabel et al. 2006; Shen et al. 2012).

The outflowing matter from quasars is detected via absorption features in their spectra, which appear in addition to the plethora of absorption features produced by intervening objects (e.g., foreground galaxies, the IGM, and clouds in the Milky Way). The former, usually called *intrinsic* absorption lines, are observed in the spectra of about half of all quasars (e.g., Vestergaard 2003; Wise et al. 2004; Misawa et al. 2007a; Nestor et al. 2008), while the latter, usually called *intervening* absorption lines, are detected in virtually all quasar spectra.

Intrinsic absorption lines are a powerful tool for probing the outflowing winds of quasars, which are difficult to observe directly (e.g., Weymann et al. 1991; Hamann et al. 1997b; Arav et al. 1999; Srianand et al. 2002; Moe et al. 2009; Capellupo et al. 2011; Filiz Ak et al. 2013). However, a drawback of most studies of intrinsic quasar absorption lines is that they probe *only* a single sightline (i.e., one dimension) toward the nucleus of each quasar, while the physical conditions of the outflow are likely to depend on the polar angle relative to the axis of the quasar (e.g., Elvis 2000; Ganguly et al. 2001). Therefore, the structure of the outflowing winds (e.g., absorber's size, kinematic motions, and volume density) is still largely unknown.

Multiple images of quasars produced by gravitational lensing provide a unique way for studying multiple sightlines through the same outflow (e.g., Turnshek et al. 2001). Lensed quasars with large image separation angles have a very good chance of revealing structural differences in the outflowing winds in the vicinity of the quasars themselves. In this sense, the following three lensed quasars are the most promising targets because they are lensed by a cluster of galaxies rather than by a single massive galaxy: SDSS J1004+4112 with a separation angle of $14\farcs6$ (Inada et al. 2003), SDSS J1029+2623 with $22\farcs5$ (Inada et al. 2006; Oguri et al. 2008), and SDSS J2222+2745 with $15\farcs1$ (Dahle et al. 2013).

* Based on data collected at the Subaru Telescope, which is operated by the National Astronomical Observatory of Japan.

Among these, SDSS J1029+2623 at $z_{\rm em} = 2.197$, the current record-holding lensed quasar whose images have the largest known angular separation, has proven to be an excellent target for the study of the structure of its outflow because there are clear absorption features detected at the blue wings of the C IV, N V, and Lyα emission lines in the spectra of the lensed images (Inada et al. 2006; Oguri et al. 2008). Misawa et al. (2013) obtained a high-resolution spectrum using the Subaru telescope and the High-Dispersion Spectrograph (HDS), and discovered several clear indications that the absorption lines indeed arise in the outflowing wind: partial coverage[9] and line locking.[10] Misawa et al. (2013) also discovered a clear difference between the broad absorption profiles in the spectra of the two lensed images.

We observed SDSS J1029+2623 again using Subaru/HDS (Misawa et al. 2014b) and the Very Large Telescope (VLT) with the Ultraviolet and Visual Echelle Spectrograph (UVES; Misawa et al. 2016) about four years (~1460 days) after the first observation (which is longer than the ~774 day time-delay between the lensed images; Fohlmeister et al. 2013). We confirmed that the difference in absorption profile persists at the 3σ level in the new spectra, which suggests that our sightlines to the lensed images are indeed passing through different regions of the outflowing wind at different angles (i.e., they are not a result of time variability due to the time delay between the images) (Misawa et al. 2014b). The size of an absorbing gas cloud, d, at a distance of r from the source should be smaller than the physical distance between the sightlines of the two lensed images, i.e., $d \leqslant r\,\theta'$, to avoid covering the cylinders of both sightlines. In the above expression $\theta' = (D_{\rm ol}/D_{\rm sl})\theta$ is the separation angle seen from the source with θ as the observed angular separation between the images and $D_{\rm ol}$ and $D_{\rm sl}$ as the angular diameter distances from the observer to the lens and from the source to the lens, respectively. This result places a direct constraint on the absorber's size in the direction perpendicular to the line of sight for the first time.

In this paper, we carry out the same type of observations for the quasar, SDSS J1001+5027, which is lensed not by a cluster of galaxies but by a single massive galaxy. Because the lensed images of this quasar have an angular separation of ~3″ (about 10 times smaller than that of SDSS J1029+2623), the cylinders of sight to the two lensed images overlap almost completely at a small distance from the source. Thus we cannot observe the structure of the outflow from two different directions. Instead, we can effectively monitor the outflow at two epochs by virtue of the time-delay between the lensed images. Among the ~150 lensed quasars that have been discovered so far in the CfA-Arizona Space Telescope LEns (CASTLE)[11] and SDSS Quasar Lens Search (SQLS)[12] surveys, only SDSS J1001+5027 satisfies all of the following criteria: (1) strong absorption troughs exist in the blue wings of broad emission lines (i.e., a promising candidate for blueshifted lines from an outflowing wind), (2) bright enough ($i < 18$), (3) the angular separation of the lensed images is at least three times the typical seeing size at MaunaKea ($\theta \gtrsim 2\farcs0$), (4) good target visibility from the Subaru telescope, and (5) good sensitivity in the optical band for the detection of C IV absorption lines at $\lambda_{\rm obs} \sim 4000$–$7000$ Å (i.e., $z_{\rm em} \sim 1.6$–3.5). Our goals are (i) to place new limits on the physical properties of the BAL absorbing clouds and their distance from the source and (ii) to identify narrow absorption lines (NALs) that originate in the outflowing wind based on identical line profiles measured in spectra of comparably high signal-to-noise ratios (hereafter S/N) from the two different sightlines.

The paper is organized as follows. We describe the detailed properties of our target SDSS J1001+5027 in Section 2 and the observations and data reduction in Section 3. The results and discussion are presented in Sections 4 and 5. Finally, we summarize our conclusions in Section 6. We use a cosmology with $H_0 = 70\,{\rm km\,s^{-1}\,Mpc^{-1}}$, $\Omega_m = 0.3$, and $\Omega_\Lambda = 0.7$ throughout the paper.

2. The Lensed Quasar SDSS J1001+5027

The quasar SDSS J1001+5027 at $z_{\rm em} = 1.838$ was first reported in Oguri et al. (2005) as a lensed quasar with two images, A ($i = 17.36$) and B ($i = 17.71$), that had been originally selected as a lens candidate from the Sloan Digital Sky Survey (SDSS; York et al. 2000). The redshift of the main lensing galaxy is spectroscopically determined as $z_l = 0.415$ (Inada et al. 2012). The image separation ($\theta = 2\farcs86$) is slightly larger than the typical value for lensed quasars by a single massive galaxy ($\theta \sim 1''$–$2''$). Oguri et al. (2005) discovered a possible second lensing galaxy and an enhancement of galaxy number density on a larger scale, within 60″ of the quasar images. These additional galaxies could contribute to the large image separation.

Given the redshifts of the lensing galaxy and the source (i.e., the quasar), the separation angle of the light rays that form the images A and B, *as seen from the source*, is evaluated as $\theta' = 1\farcs37$, which is almost half the separation angle seen from our position. The time delay between the images has also been measured. Rathna Kumar et al. (2013) monitored the optical R-band light curves of images A and B with measurements at 443 independent epochs for more than six years, and concluded that image A leads B by 119.3 ± 3.3 days after combining results from five different methods.[13] Rusu et al. (2016) also obtained several possible mass models for the lensing object and determined a total magnification factor $\mu = 3.51$[14] of the quasar images. Because the flux ratio of images A and B is 1:0.77 (Oguri et al. 2005), we will use $\mu_{\rm A} = 1.99$ and $\mu_{\rm B} = 1.52$ as magnification factors for images A and B, respectively, throughout the paper.

Here, we estimate some of the physical parameters of the quasar that will be useful in our later discussion on our results. We first estimate the sizes of the broad emission line region (BELR), $R_{\rm BELR}$, and the continuum source, $R_{\rm cont}$, following Misawa et al. (2013). The former is calculated using the empirical relation between $R_{\rm BELR}$ and quasar luminosity (McLure & Dunlop 2004). The monochromatic luminosity of image A at $\lambda_r = 3000$ Å in the quasar rest-frame is measured by Shen et al. (2011) as $\log \lambda L_{3000} = 46.52 \pm 0.01$ erg s^{-1}.

[9] Absorbers do not cover the background flux source completely along our sightline.

[10] The red component of a doublet (such as C IV, Si IV, and N V) is aligned with a blue component of the following doublet, which is a signature of a radiatively driven wind and only detectable if our sightline is almost parallel to the wind streamlines (Benn et al. 2005; Bowler et al. 2014).

[11] https://www.cfa.harvard.edu/castles/

[12] http://www-utap.phys.s.u-tokyo.ac.jp/~sdss/sqls/

[13] Aghamousa & Shafieloo (2017) also evaluated the time delay as $117^{+7.1}_{-3.7}$ days based on their own algorithm, which is in good agreement with the result by Rathna Kumar et al. (2013).

[14] This is a weighted average of magnification factors for their 13 mass models.

Table 1
Log of Observations

Target	R.A. (hh mm ss)	Decl. (dd mm ss)	m_i (mag)	Obs Date	R	T_{exp} (s)	S/N[a] (bin^{-1})
SDSS J1001+5027 A	10 01 28.61	+50 27 56.9	17.36	2016 Jan 27	45000	12000	16
				2017 Jan 19	45000	14400	15
SDSS J1001+5027 B	10 01 28.35	+50 27 58.5	17.71	2016 Jan 27	45000	12000	11
				2017 Jan 19	45000	12000	9

Note.
[a] Signal-to-noise ratio at $\lambda_{obs} \sim 4500$ Å.

After correcting for magnification, we estimate $R_{BELR} \sim 0.4^{+0.7}_{-0.3}$ pc, where the main source of uncertainty is the scatter in the empirical relation in McLure & Dunlop (2004). As for the size of the continuum source, we take five times the Schwarzschild radius ($5R_S = 10GM_{BH}/c^2$), following Misawa et al. (2005), where M_{BH} is the mass of the central black hole of the quasar. Recent microlensing studies suggest that the size of the continuum source is larger than the estimate based on the Shakura–Sunyaev disk model (Shakura & Sunyaev 1973) by a factor of four (e.g., Morgan et al. 2010, see also the discussion in Rodríguez Hidalgo et al. 2013). In this paper, however, we use the original value without correcting it so as to compare the results of our current target SDSS J1001+5027 to those of our previous target SDSS J1029+2623 (Misawa et al. 2013, 2014b, 2016). The virial mass of the central black hole is already calculated in Shen et al. (2011). After correcting for magnification, we obtain a black hole mass of $\log(M_{BH}/M_\odot) = 9.66 \pm 0.06$ and a continuum source size of $R_{cont} = (2.2 \pm 0.3) \times 10^{-3}$ pc, about 170 times smaller than R_{BELR}. The Eddington ratio of the quasar corresponding to the above values is $L/L_E \sim 0.15$, which is a value of typical bright quasars, $L/L_E \sim 0.07$–1.6 (Netzer et al. 2007).

Based on the separation angle seen from the source, θ', and the size of sources, R_{BELR} and R_{cont}, we are also able to calculate the boundary distance, r_b, i.e., the distance from the source where the two cylinders of sight for an extended object corresponding to the two images become fully separated with no overlap as introduced in Misawa et al. (2013). The boundary distance for SDSS J1001+5027 is $r_b = 330^{+50}_{-40}$ pc if only the continuum source is the flux source or 60^{+100}_{-40} kpc if the BELR is also part of the background source. Both of these are considerably larger than those evaluated for the large-separation lensed quasar SDSS J1029+2623 (~3.5 pc and ~1.2 kpc, respectively; see Misawa et al. 2016).

3. Observations and Data Reduction

We conducted high-resolution spectroscopic observations of the two images of the lensed quasar SDSS J1001+5027 using Subaru/HDS on 2016 January 27 and 2017 January 19 (epochs E1 and E2, hereafter) whose time separation (~358 days) is larger than the time delay between the images (~119 days) in the observed frame. We used a slit width of 0.″8, which yielded a resolving power of $R \sim 45{,}000$. The wavelength coverage is 3820–4600 Å on the blue CCD and 4680–5490 Å on the red CCD, which includes the Si IV, C IV, and C III] emission lines at the redshift of this quasar. Because the spectra were oversampled (i.e., there were 8 pixels per resolution element), we binned every 4 pixels in both spatial and dispersion directions (i.e., ~0.05 Å per bin) to increase the S/N. The sky conditions were good. The total integration time was 12,000 s for each image in each epoch, except for image B in epoch E1 whose integration time was slightly longer, ~14400 s.

We reduced the data in a standard manner with the IRAF software.[15] Wavelength calibration was performed with the help of a Th–Ar lamp spectrum. We carried out the flux calibration of the spectra using the spectrum of the spectrophotometric standard star Feige 34. The final S/N is about 9–16 bin^{-1} at 4500 Å. The log of the observations is presented in Table 1.

4. Results

We show normalized spectra over the full wavelength range of our observations for images A and B in Figure 1. These spectra were binned every 0.5 Å for display purposes, and the 1σ errors are also shown. Because the blue wing of the C IV emission line is severely absorbed at $\lambda \sim 4300$ Å, we cannot fit the continuum in that region directly. Instead, we model the continuum and emission line profile using a power law and two Gaussian profiles for the broad and narrow C IV emission components (Figure 2), which is a standard practice. We do not consider the He II λ1640 emission line that is located about 250 Å redward of the C IV emission line, because its contribution to the blue wing of the C IV emission line is negligible. The best-fitting models are very similar for the four spectra; FWHMs of broad and narrow emission components are 5890 ± 390 km s^{-1} and 1180 ± 125 km s^{-1}, respectively, which are close to the typical values of optically bright quasars at $z \sim 2$, ~4900 km s^{-1} and ~1400 km s^{-1} (e.g., Brotherton & Wills 1994; Marziani et al. 1996; Sulentic et al. 2017, and references therein).

In addition to the broad absorption feature above, we also detect narrower absorption features whose confidence level is greater than 5σ in the normalized spectra of images A and B in both epochs E1 and E2, using the line detection code SEARCH, written by Chris Churchill. We first identify doublet lines including C IV and Mg II in the regions between the bluest edge of the observed spectrum ($\lambda \sim 3820$ Å) and the corresponding emission lines. In total, we identified one Mg II and three C IV systems in the image A spectrum, and two Mg II and three C IV systems in the image B spectrum in both epochs. At the redshift of these systems, we also detected 11 single metal absorption lines (Si II λ1527, Fe II λ1608, Al II λ1671, Al III λ1855, Al III λ1863, Fe II λ2344, Fe II λ2374, Fe II λ2383, Fe II λ2587, Fe II λ2600, and Mg I λ2853), as summarized in Table 2. The Mg II system at the redshift of the lensing galaxy ($z_{abs} \sim 0.415$) is detected only in the image B spectrum, which is probably why the image B

[15] IRAF is distributed by the National Optical Astronomy Observatories, which are operated by the Association of Universities for Research in Astronomy, Inc., under cooperative agreement with the National Science Foundation.

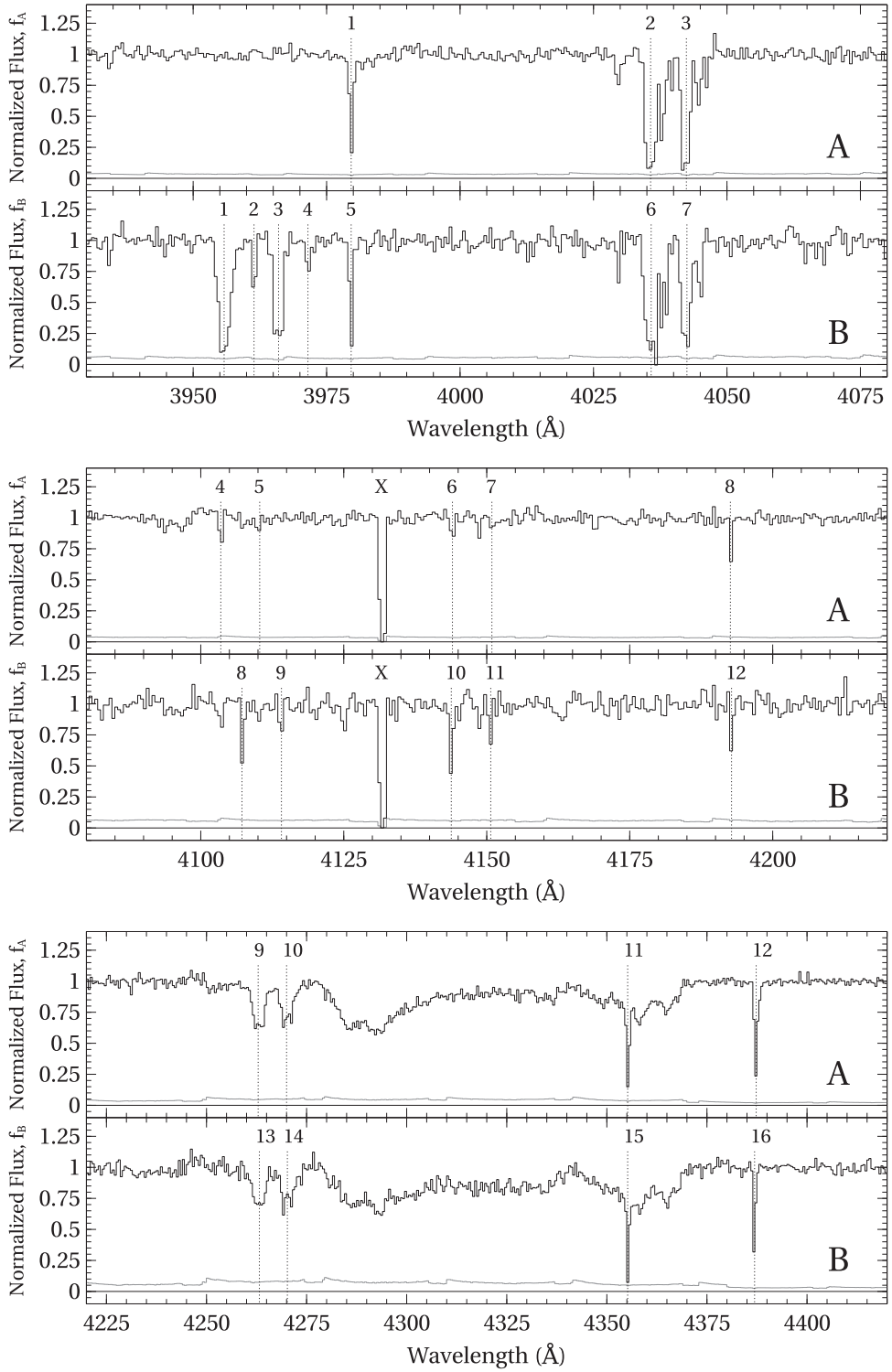

Figure 1. Normalized spectra and their 1σ errors (lower traces) for images A and B of SDSS J1001+5027 in epoch E1, taken with Subaru/HDS, after sampling every 0.5 Å for display purposes only. Identification numbers from Table 2 are shown above the corresponding absorption lines. Crosses denote data defects such as bad columns and bad pixels.

spectrum is redder compared to the image A spectrum, as noted in Oguri et al. (2005).

4.1. Broad Absorption Line

The broad P-Cygni profile of the C IV emission line was known from medium resolution spectra ($R \sim 2000$) of the quasar (Oguri et al. 2005). This broad absorption feature with FWHM of $\sim$7000 km s^{-1} appears fairly smooth in our high-resolution spectrum, which means that the feature is indeed intrinsically broad and smooth and cannot be attributed to intervening absorbers whose typical line width is much smaller (i.e., up to several hundreds of km s^{-1}).

Because this feature satisfies the definition of a broad absorption line (BALs), with more than 10% of the flux absorbed over at least a 2000 km s^{-1} range continuously (Weymann et al. 1991), we refer

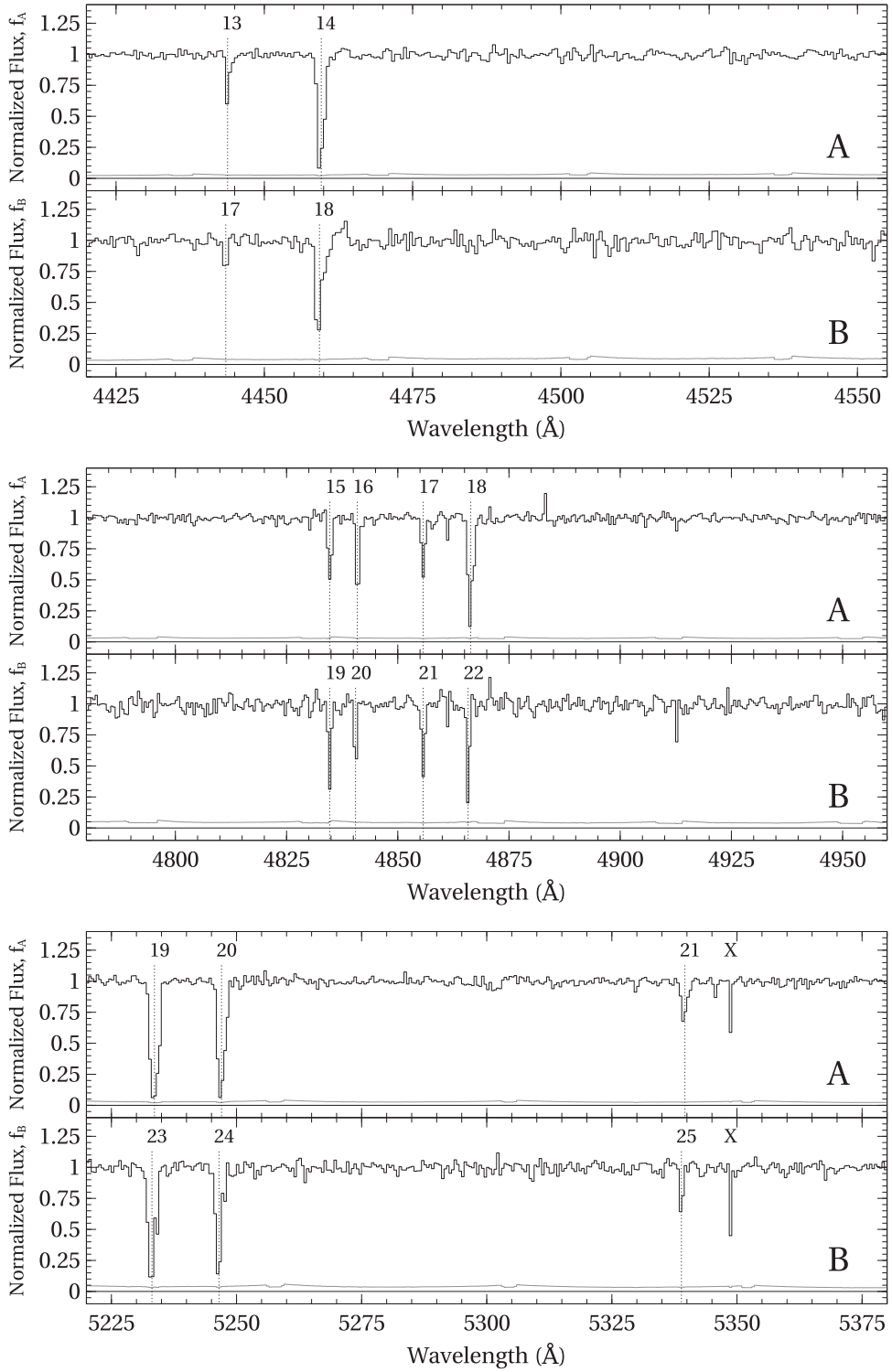

Figure 1. (Continued.)

to it as a BAL, hereafter. Corresponding BAL features in lines other than C IV are not detected at the same redshift in our spectra, although the wavelength region corresponding to the Si IV BAL is severely affected by bad CCD columns.[16] In a UV spectrum of the quasar taken with *HST*/COS, Moravec et al. (2017) also detected O VI (and possibly P V) BALs. The offset velocity from the quasar emission redshift along the line of sight (i.e., the apparent ejection velocity) of the C IV BAL is $v_{\rm ej} \sim 2500$–9500 km s^{-1} (positive values correspond to blueshifts).

Examining the C IV BAL in more detail, we note that the feature consists of three separate troughs; one narrow and two broader components. We will call these BAL components c1, c2, and c3, as shown in Figure 3. Only component c1 has the blue and red members of the doublet unblended from each

[16] There is no obvious broad absorption feature detected in intermediate resolution spectra ($R \sim 2000$) at which Si IV BAL is expected to be located (Moravec et al. 2017).

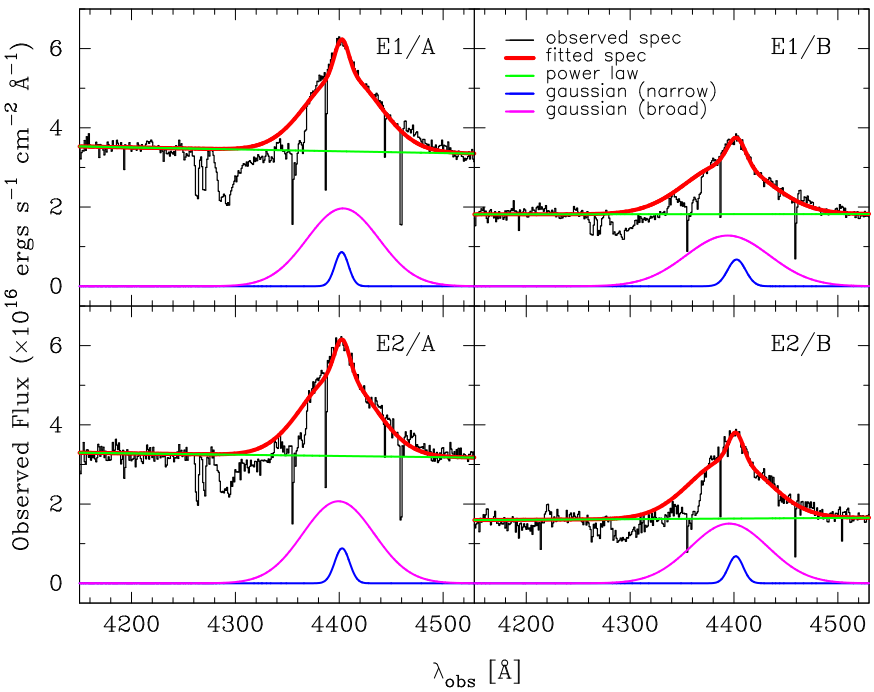

Figure 2. Flux calibrated spectra around the C IV emission lines of images A and B of the quasar SDSS J1001+5027 in epoch E1 (upper left and right) and epoch E2 (lower left and right), with multi-component fits using two Gaussian components (i.e., broad and narrow emission lines) and power law (i.e., the continuum level). The green line shows the continuum fit, the magenta and blue lines show the two Gaussian components and the thick red line shows the sum of all of the above.

other. A sharp feature in component c3 at $\lambda \sim 4355$ Å is not part of the BAL feature but is instead an Al II λ1671 line from an intervening absorber at $z_{\rm abs} = 1.6067$.

We also monitored the variability of the absorption profile and strength of the C IV BAL using spectra in two epochs whose time separation is 358 days in the observed frame (i.e., ~126 days in the quasar rest frame). Because the two cylinders of sight to the two lensed images overlap completely at the distance of the absorber (as we demonstrate later in Section 5.1), we effectively monitored the same absorber at four epochs using the observations of the two lensed images in two epochs; the relative time intervals of the four epochs are $\Delta t_{\rm obs} = 0$, 119, 358, and 476 days.

We evaluated the equivalent width (EW) of the C IV BAL with its 1σ error, σ(EW), in our four spectra, to search for variability. Because our measurements of EW suffer not only photon noise ($\sigma_{\rm phot}$) but also uncertainties in the placement of the continuum level ($\sigma_{\rm cont}$), we combine these two errors in quadrature to obtain the final 1σ error. Following Misawa et al. (2014a), the latter error is calculated empirically as

$$\sigma_{\rm cont}({\rm EW}) = \frac{(\lambda_{\rm max} - \lambda_{\rm min})}{2\,({\rm S/N})}, \quad (1)$$

where $\lambda_{\rm max} - \lambda_{\rm min}$ is the wavelength width of the C IV BAL (see the discussion in Misawa et al. 2014a).

We do not find clear variability in the total EW of the C IV BAL between observing epochs, although there is a small difference between images A and B in epoch E2 as shown in Figure 4(a). However, once we separate the BAL feature into three components and measure their EW separately, we note that the broader components c2 and c3 show clear variability between epochs (see Figures 3 and 4(b)). It appears that the EW of the component c2 first decreased in 358 days and then increased in 119 days, while that of component c3 is almost stable in the first 358 days but suddenly increased in 119 days. Thus, the variability pattern is not synchronized. We will discuss a plausible scenario to explain this behavior in the following section.

Of three components of the C IV BAL, only component c1 has the blue and red members of the doublet unblended, which enables us to apply partial coverage analysis. We examine the optical depth ratio of the doublet lines to see if it deviates from the value of 2:1 prescribed by atomic physics. Attributing any such deviation to dilution of absorption troughs by unocculted light from the background source allows us to find the fraction of the projected area of the source that is occulted by the absorber (e.g., Wampler et al. 1995; Barlow & Sargent 1997; Hamann et al. 1997b; Ganguly et al. 1999). We can evaluate a covering factor ($C_{\rm f}$), a fraction of background light occulted by the absorber, by using the equation,

$$C_{\rm f}(\lambda) = \frac{[1 - R_r(\lambda)]^2}{1 + R_b(\lambda) - 2R_r(\lambda)}, \quad (2)$$

where R_b and R_r are the continuum normalized intensities of the stronger (bluer) and weaker (redder) members of the doublet (see, for example, Barlow & Sargent 1997). We evaluate $C_{\rm f}$ values for each *bin* (not for each absorption component) as done in Ganguly et al. (1999). We can also use the line fitting software package MINFIT (Churchill 1997; Churchill et al. 2003) to fit absorption profiles with four parameters; absorption redshift ($z_{\rm abs}$), column density ($\log N$ in cm^{-2}), Doppler parameter (b in km s^{-1}), and covering factor ($C_{\rm f}$). If MINFIT gives unphysical covering factors for some components, we rerun the code assuming $C_{\rm f} = 1$ for those components following Misawa et al. (2005). As an example, the fitting result for the image A spectrum in epoch E1 by both methods

Table 2
Narrow Absorption Lines in Epoch E1

Ion	Image A			Image B					
	z_{abs}	EW_{obs}[a] (Å)	ID	z_{abs}	EW_{obs}[a] (Å)	ID	$D_{\perp}$[b] (pkpc)	Δv[c] (km s^{-1})	$\lvert\Delta$ EW$\rvert$[d] (Å)
Mg IIλ2796	⋯	⋯		0.4147	2.205 ± 0.150	1	15.7	⋯	⋯
Mg IIλ2803	⋯	⋯			1.663 ± 0.124	3			⋯
Mg IIλ2796	⋯	⋯		0.4166	0.352 ± 0.043	2	15.7	⋯	⋯
Mg IIλ2803	⋯	⋯			0.214 ± 0.042	4			⋯
Mg IIλ2796	0.8716	1.949 ± 0.058	19	0.8714	1.656 ± 0.105	23	7.0	32.1	0.293 ± 0.120
Mg IIλ2803		1.638 ± 0.055	20		1.279 ± 0.090	24			0.359 ± 0.105
Fe IIλ2344		0.806 ± 0.046	12		0.529 ± 0.050	16			0.277 ± 0.068
Fe IIλ2374		0.283 ± 0.025	13		0.213 ± 0.050	17			0.070 ± 0.056
Fe IIλ2383		1.271 ± 0.051	14		1.029 ± 0.096	18			0.242 ± 0.109
Fe IIλ2587		0.557 ± 0.030	16		0.414 ± 0.057	20			0.143 ± 0.064
Fe IIλ2600		1.134 ± 0.048	18		0.648 ± 0.080	22			0.486 ± 0.093
Mg Iλ2853		0.457 ± 0.042	21		0.322 ± 0.036	25			0.135 ± 0.055
C IVλ1548	1.6067	3.076 ± 0.171	2	1.6067	3.213 ± 0.264	6	1.0	0.0	0.137 ± 0.315
C IVλ1551		2.307 ± 0.160	3		2.190 ± 0.232	7			0.117 ± 0.282
Si IIλ1527		0.664 ± 0.036	1		0.628 ± 0.045	5			0.036 ± 0.058
Fe IIλ1608		0.183 ± 0.022	8		0.235 ± 0.057	12			0.052 ± 0.061
Al IIλ1671[e]		0.677 ± 0.031	11		0.670 ± 0.046	15			0.007 ± 0.055
Al IIIλ1855		0.525 ± 0.038	15		0.567 ± 0.069	19			0.042 ± 0.079
Al IIIλ1863		0.445 ± 0.034	17		0.522 ± 0.062	21			0.077 ± 0.071
C IVλ1548	1.6505	0.149 ± 0.034	4	1.6530	0.248 ± 0.042	8	0.8	−282.8	0.099 ± 0.054
C IVλ1551		0.060 ± 0.016	5		0.149 ± 0.032	9			0.089 ± 0.036
C IVλ1548	1.6766	0.129 ± 0.028	6	1.6766	0.386 ± 0.053	10	0.7	0.0	0.257 ± 0.060
C IVλ1551		0.070 ± 0.023	7		0.219 ± 0.050	11			0.149 ± 0.055
C IVλ1548[f]	1.7535	1.208 ± 0.149	9	1.7536	1.069 ± 0.205	13	0.3	−10.9	0.139 ± 0.253
C IVλ1551[f]		1.109 ± 0.192	10		0.993 ± 0.234	14			0.116 ± 0.303

Notes.
[a] Observed-frame equivalent width.
[b] Physical distance between two sightlines in the transverse direction.
[c] Velocity offset between NALs detected in images A and B ($v_{ej}(z_B) - v_{ej}(z_A)$).
[d] Equivalent width difference between NALs detected in images A and B.
[e] This line is blended with C IV BAL.
[f] This line is probably a part of C IV BAL.

is shown in Figure 5. The fit parameters for all four spectra are summarized in Table 3. Although the number of absorption components needed to fit the absorption profile depends on the S/N of each spectrum (from eight components for image A in epoch E1 to only one component for image B in epoch E1), the covering factors evaluated for each bin and for each absorption component are always consistent with each other in all spectra. This result gives us confidence that component c1 shows partial coverage with $C_f \sim 0.3$, which is smaller than the value evaluated for O VI BAL detected in the UV spectrum ($C_f \sim 0.67$; Moravec et al. 2017).

4.2. Narrow Absorption Lines

While BALs are very likely physically associated with quasars, NALs are more difficult to classify as intrinsic or intervening. There are several reliable criteria to distinguish intrinsic NALs from intervening NALs including time variability, line locking, and partial coverage (e.g., Barlow & Sargent 1997; Hamann et al. 1997b). Among these, the first two are applicable to our spectra, while we cannot use partial coverage analysis because our NALs are detected in regions of our spectra where the S/N is low.[17] None of the NALs show time variability (with one possible exception below) or line locking, while both of these effects are seen in several NALs in the spectra of the large-separation lensed quasar SDSS J1029+2623 (Misawa et al. 2016).

In addition to these three methods of identifying intrinsic NALs, Misawa et al. (2016) introduced a new method by exploiting multi-sightline observations. If NALs with identical line profiles are detected at the same redshift (i.e., at a common apparent ejection velocity from the quasar) along two sightlines with a large physical distance in the transverse direction, the corresponding absorber is very likely to be intrinsic to the quasar, because both cylinders of sight to the two lensed images can go through the same gas parcels only if these parcels are located in the vicinity of the flux source. For example, if an absorber is located at a distance of ∼1 pc from

[17] We can apply the analysis only for component c1 of the C IV BAL above because of its simple and deep absorption profile located in a higher S/N region.

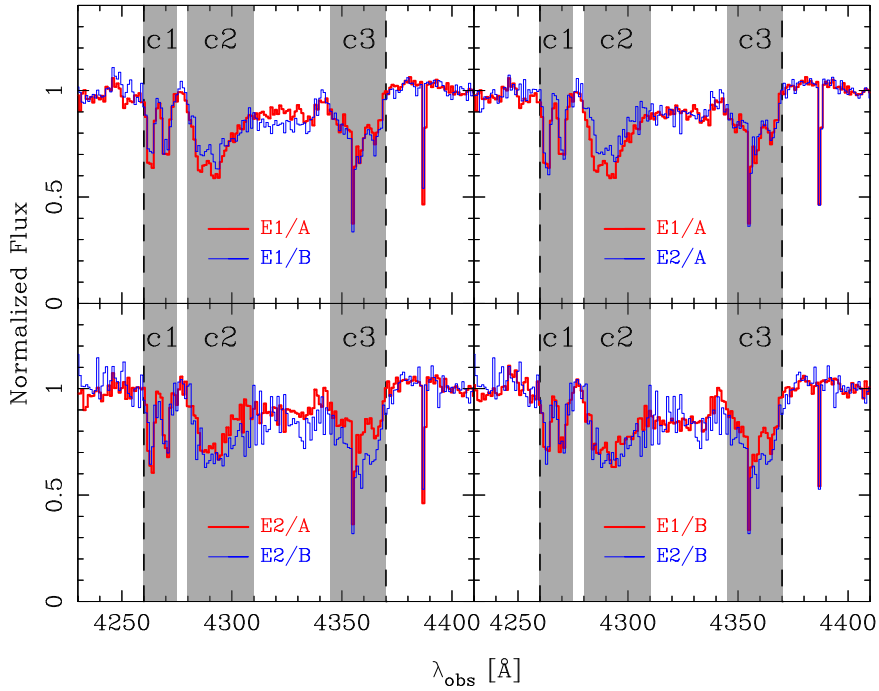

Figure 3. Comparison of C IV BAL profiles in the normalized spectra between image A and B in epoch E1 (upper left) and E2 (lower left) and between image A (upper right) and image B (lower right) in epochs E1 and E2. Three shaded areas denote the components c1, c2, and c3.

the source, the physical separation between the two sightlines ($\sim 10^{-5}$ pc) is smaller than the typical size of a clump in the outflow, $d \sim 10^{-4}$ pc, as estimated in Hamann et al. (2013). However, this method is effective only if (i) it is applied to *metal* absorption lines such as C IV and Mg II NALs,[18] (ii) the NALs to be compared are detected in the same quality spectra (i.e., same spectral resolution, S/N, and sampling), and (iii) the physical distance between two sightlines in the transverse direction at the apparent redshift of the absorber is comparable to or larger than the typical size of the metal absorbers (i.e., $\sim$0.05–5 kpc; Stern et al. 2016).[19] Our spectra of SDSS J1001+5027 satisfy all of these requirements. Although some NAL pairs are detected at almost the same redshift along the two sightlines, their line profiles are clearly different from each other. Since none of the NAL profiles match between sightlines A and B toward SDSS J1001+5027, we cannot identify any of the 6 NAL systems detected in the spectra as intrinsic ones based only on this method.

Only the Mg I NAL of the Mg II absorption system at $z_{abs} = 0.8716$ shows a hint of time variability with differences at the $\sim 4\sigma$ significance level near the minimum of the line profile. The profile appears to become narrower in $\Delta t_{obs} = 358$ days ($\Delta t_{rest} = 191$ days at $z_{abs} = 0.8716$) between epochs E1 and E2 (Figure 6). However, the detection of variability is marginal because there are several noise spikes in the spectra near the Mg I NAL with a similar significance level of variability. We need higher quality spectra to confirm the Mg I variability. It is also remarkable that all NALs in the system at $z_{abs} = 0.8716$, including the Mg I NAL, show a velocity offset in the sense that NALs in image A are redshifted from those in image B between two sightlines with a projected separation of $\sim$7 kpc (Figure 7). We computed the flux-weighted line center as the first moment of the line profile for each NAL in the spectra of both images, and found that the line centers in both spectra have substantial offset velocities with $\Delta v = 30 \pm 8$ km s^{-1}. We interpret both the *marginal* Mg I variability and the velocity offset as the result of motion of gas within or around a foreground galaxy at $z_{abs} = 0.8716$. For example, the NAL system could originate in gas clouds that are tidally stripped by a galaxy merger or accreting onto or outflowing from a foreground galaxy. This would be one of only a few cases in which NALs of low-ionization species show any time variability (e.g., Hacker et al. 2013, and references therein).

5. Discussion

5.1. Broad Absorption Line

The C IV BAL shows variability in profile and strength between the two observing epochs along both sightlines. There are at least three possible origins for the variability; gas motion across our sightline (e.g., Gibson et al. 2008; Hamann et al. 2008; Vivek et al. 2012, 2014, 2016; Krongold et al. 2017), a change of ionization state of the absorber (e.g., Misawa et al. 2007b; Hamann et al. 2011; Arav et al. 2012; Filiz Ak et al. 2013; Trevese et al. 2013; Horiuchi et al. 2016), and a microlensing event (e.g., Green 2006). Among these, the last one is less likely because the microlensing effect of BELs in SDSS J1001+5027 is almost negligible (Guerras et al. 2013).

[18] H I absorbers in the IGM (i.e., Lyα forest) have a much larger projected size ($\sim$1 Mpc) than the physical distance between two lines of sight to SDSS J1001+5027 ($\sim$1–10 kpc; see Table 2).

[19] Intervening galaxies and their circumgalactic media (CGM) are the main intervening metal absorption line systems. Although the typical extent of the CGM from galaxies is $\sim$200–300 kpc (e.g., Chen et al. 2001; Churchill et al. 2013; Turner et al. 2014), their covering factor is not unity (i.e., they have an inhomogeneous internal structure; e.g., Kacprzak et al. 2012; Bordoloi et al. 2014; Koyamada et al. 2017). The typical size of each clump is estimated to be $\sim$4 kpc or $\sim$50 pc for Si IV and Mg II absorbers, respectively (Stern et al. 2016). We can use the Si IV absorber size as a proxy for the C IV absorber size because of its similar ionization potential. Even if two cylinders of sight to the two lensed images pass through a single cloud, the corresponding absorption line profiles in their spectra are not identical because their total column densities are unlikely to be same (e.g., one goes through the middle of the cloud, while the other does not).

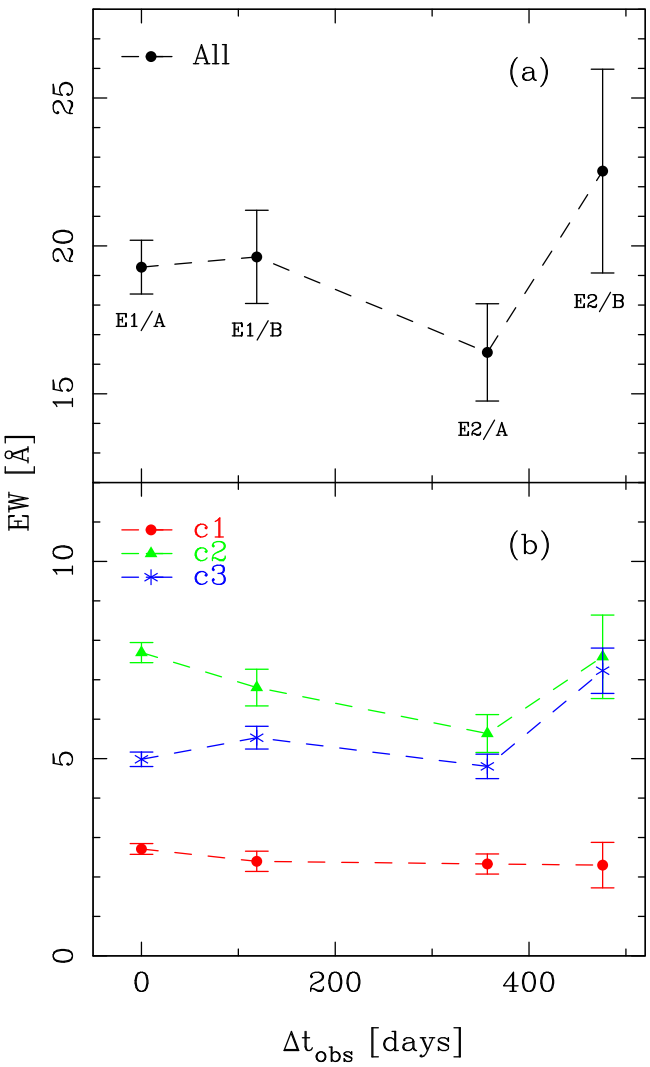

Figure 4. Monitoring result for EWs of the whole range of the C IV BAL (top) and each component (bottom). The horizontal axis is the time delay from the first epoch in the observed frame (in days). The vertical axis is the observed EWs (with 1σ errors).

The observed variability trends can place further constraints on the possible scenarios. The time variability is seen in only portions of the C IV BAL and its variability pattern depends on the absorber's ejection velocity from the source (Figure 3). A change of incident ionizing flux, which would affect all components in concert, is clearly inconsistent with the observed behavior. In principle, the ionization state of the absorber could change because of changes in its density due to expansion or compression but such changes are very slow in view of the local sound speed. We estimate the sound speed to be $c_s \sim 10\ T_4^{1/2}\ \mathrm{km\,s^{-1}}$, where T_4 is the temperature scaled by 10^4 K, which is a typical value of the temperature of a photoionized gas. Using the covering factor evaluated above and assuming conservatively that only the continuum source is covered by the absorber we find that the absorber size is $a > C_\mathrm{f}\ R_\mathrm{cont} \sim 7 \times 10^{-4}$ pc. Hence the characteristic time for changes in the density due to internal motions in the absorber is $\geqslant$70 years, which is two orders of magnitude longer than the observed variability timescale. The mismatch in timescales remains significant even if we attribute different troughs of the profile to different portions of the absorber; such portions must be substantial fractions of the entire absorber, as the profile comprises only three troughs. Therefore, as the most plausible and natural explanation, we take the bulk gas motion scenario that is typically adopted in the case that variability occurs in just a portion of BAL profiles like SDSS J1001+5027 (e.g., Gibson et al. 2008; Hamann et al. 2008; Capellupo et al. 2013).

In our preferred scenario for the variability, the absorber is moving either in front of the continuum source or in front of the BELR at the local dynamical speed. The latter is implausible because it would imply a transverse (i.e., rotational) velocity greater than the speed of light, namely $v_\mathrm{rot} \geqslant R_\mathrm{BELR}/\Delta t_\mathrm{rest} > c$. Thus, the continuum source is the only plausible background source in this context, and the inferred rotational velocity is $v_\mathrm{rot} \geqslant R_\mathrm{cont}/\Delta t_\mathrm{rest}$. Taking $\Delta t_\mathrm{rest} = 42$ days, the interval over which the most substantial EW variation is observed (see Figure 4), we find that $v_\mathrm{rot} \geqslant 18{,}200\ \mathrm{km\,s^{-1}}$. Assuming Keplerian motion, the absorber's distance is then $r \leqslant 0.06$ pc. Based on intermediate resolution spectra ($R \sim 2000$), Moravec et al. (2017) also discovered variability in the C IV BAL strength at the 4σ confidence level on a timescale of $\sim$0.29 years in the quasar rest frame, which gives a limit on the absorber's distance ($r < 0.4$ pc), which is consistent with our estimate. According to this estimate, the absorber is in the inner parts of the BELR. Moreover, if we assume that the absorber's observed velocity offset is indeed its outflow velocity, then the absorber is bound to the black hole.

The inferred absorber distance is much smaller than the boundary distance of the continuum source ($r_\mathrm{b} \sim 325$ pc). Thus, the cylinders of sight to the two lensed images overlap almost completely at the absorber's distance. In other words, they represent a common sightline, and we have indeed monitored the BAL profile at four epochs.

A consequence of this scenario is that an absorber so close to the ionizing source should be highly ionized unless its density is also quite high. For example, the volume density of the BAL absorber is required to be $n_\mathrm{e} \sim 10^{13}\ \mathrm{cm^{-3}}$, if we assume a typical value of the ionization parameter for the C^{3+} ion ($\log U \sim -1.7$) (Hamann et al. 1995). This is much larger than the expected value (e.g., $n_\mathrm{e} \sim 10^8\ \mathrm{cm^{-3}}$ in a mini-BAL absorber; Hamann et al. 2013). Nonetheless, there are known cases of dense absorbers located very close to the ionizing continuum source, e.g., Arp 102B (Eracleous et al. 2003) and FIRST J104459.6+365605 (de Kool et al. 2001). Another possibility is that there exists some shielding material between the continuum source and the absorber. The shielding material could be the warm absorber frequently detected in X-ray spectroscopy (e.g., Gallagher et al. 2002; Krongold et al. 2007).

5.2. Narrow Absorption Lines

There are three non-associated C IV NAL systems along both of the two sightlines toward SDSS J1001+5027 (C IV pairs, hereafter). These are systems with apparent ejection velocities greater than 5000 $\mathrm{km\,s^{-1}}$ from the quasar emission redshift (e.g., Weymann et al. 1979). In Misawa et al. (2016), we also detected 11 non-associated C IV pairs toward the large-separation lensed quasar SDSS J1029+2623 (Misawa et al. 2016). Among these 14 C IV pairs, some could still be physically associated with the quasars even if their ejection velocity is greater than 5000 $\mathrm{km\,s^{-1}}$. Indeed, Misawa et al. (2007a) estimated that about 20% of non-associated C IV NALs are intrinsic to quasars based on a covering factor analysis. However, we found that no C IV pairs have common absorption

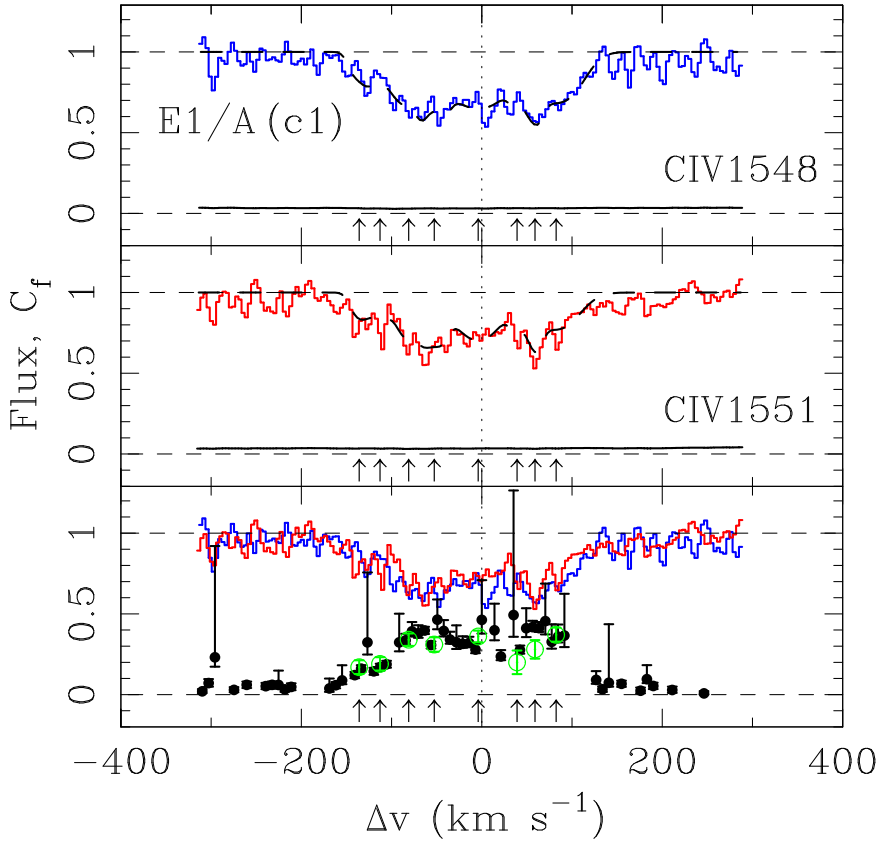

Figure 5. Results of partial coverage analysis applied to the component c1 of the C IV BAL detected in image A of SDSS J1001+5027 in epoch E1. The horizontal axis denotes the relative velocity from the flux-weighted center of the system (Δv), while the vertical axis is the normalized flux. The first two panels show the profiles of the blue and red members of a doublet (blue and red histograms) with the model profile produced by MINFIT superposed (dashed line). The positions of the absorption components are marked with upward arrows in the bottom of each panel. The bottom panel shows the covering factors with their 1σ errors, measured for each narrow component by MINFIT (green circles) or for each bin (black dots).

Table 3
Line Parameters of C IV BAL

Epoch/ Image[a]	z_{abs}[b]	v_{ej}[c] (km s^{-1})	log N (cm^{-2})	b[d] (km s^{-1})	C_f[e]
E1/A	1.7524	9507	14.12 ± 0.31	7.8 ± 2.0	$0.17^{+0.04}_{-0.04}$
	1.7526	9484	14.02 ± 0.17	11.2 ± 2.6	$0.19^{+0.04}_{-0.04}$
	1.7529	9452	14.12 ± 0.09	13.2 ± 1.5	$0.34^{+0.04}_{-0.04}$
	1.7531	9424	14.45 ± 0.19	10.8 ± 1.4	$0.31^{+0.05}_{-0.05}$
	1.7536	9375	14.35 ± 0.06	27.6 ± 3.2	$0.36^{+0.04}_{-0.04}$
	1.7540	9332	13.95 ± 0.30	7.3 ± 2.6	$0.20^{+0.08}_{-0.08}$
	1.7541	9312	14.20 ± 0.43	5.7 ± 1.8	$0.28^{+0.06}_{-0.06}$
	1.7544	9289	14.12 ± 0.10	29.2 ± 3.3	$0.37^{+0.05}_{-0.04}$
E1/B	1.7536	9373	15.53 ± 0.15	72.3 ± 6.0	$0.29^{+0.05}_{-0.05}$
E2/A	1.7531	9431	14.60 ± 0.09	37.6 ± 3.5	$0.31^{+0.05}_{-0.05}$
	1.7534	9395	16.63 ± 3.23	10.6 ± 6.0	$0.14^{+0.06}_{-0.06}$
	1.7542	9306	14.57 ± 0.05	45.2 ± 2.4	$0.42^{+0.05}_{-0.05}$
E2/B	1.7536	9375	13.90 ± 0.21	25.0 ± 3.2	$0.63^{+0.25}_{-0.20}$
	1.7542	9311	16.26 ± 2.72	9.2 ± 4.8	$0.36^{+0.09}_{-0.09}$

Notes.
[a] Observed epoch (E1/E2) and lens image (A/B).
[b] Redshift of flux-weighted line center.
[c] Ejection velocity from quasar emission redshift.
[d] Doppler parameter.
[e] Covering factor.

profiles, which means all C IV systems (even if some of them are physically associated with the quasar) are located further from the source than the boundary distance, r_b. Nonetheless, if some systems are intrinsic to the quasar, these results would be consistent with the geometrical model of the outflowing wind in Misawa et al. (2014b, 2016), in which broader absorption systems like BALs are located at $r \leqslant r_b$, while intrinsic NALs are at $r \gg r_b$. As for NALs with a large ejection velocity, only the continuum source can be the background source because their position in the spectrum is far away from the corresponding BELs. We detected neither time variability (with one possible exception discussed in the next paragraph) nor line locking of any NAL systems as signs of intrinsic absorption lines in the non-associated lines in our spectra of SDSS J1001+5027. The latter suggests our sightline is not parallel to the outflow wind that is radiatively accelerated with resonance line absorption even if some of them are intrinsic to the quasar. This is in contrast to the variable, intrinsic NALs found in quasar SDSS J1029+2623 (Misawa et al. 2013, 2016).

The only absorption line that shows a hint of time variability in both strength and profile is the Mg I NAL of the Mg II absorption system at $z_{abs} = 0.8716$ (Figure 6). This system is less likely to be intrinsic to the quasar because its offset velocity from the quasar ($v_{ej} \sim 118{,}000$ km s^{-1}) is quite large. Until now, there were only a few cases of variable intervening absorption lines with large offset velocities of $v_{ej} > 66{,}000$ km s^{-1} (Hacker et al. 2013, and references therein).

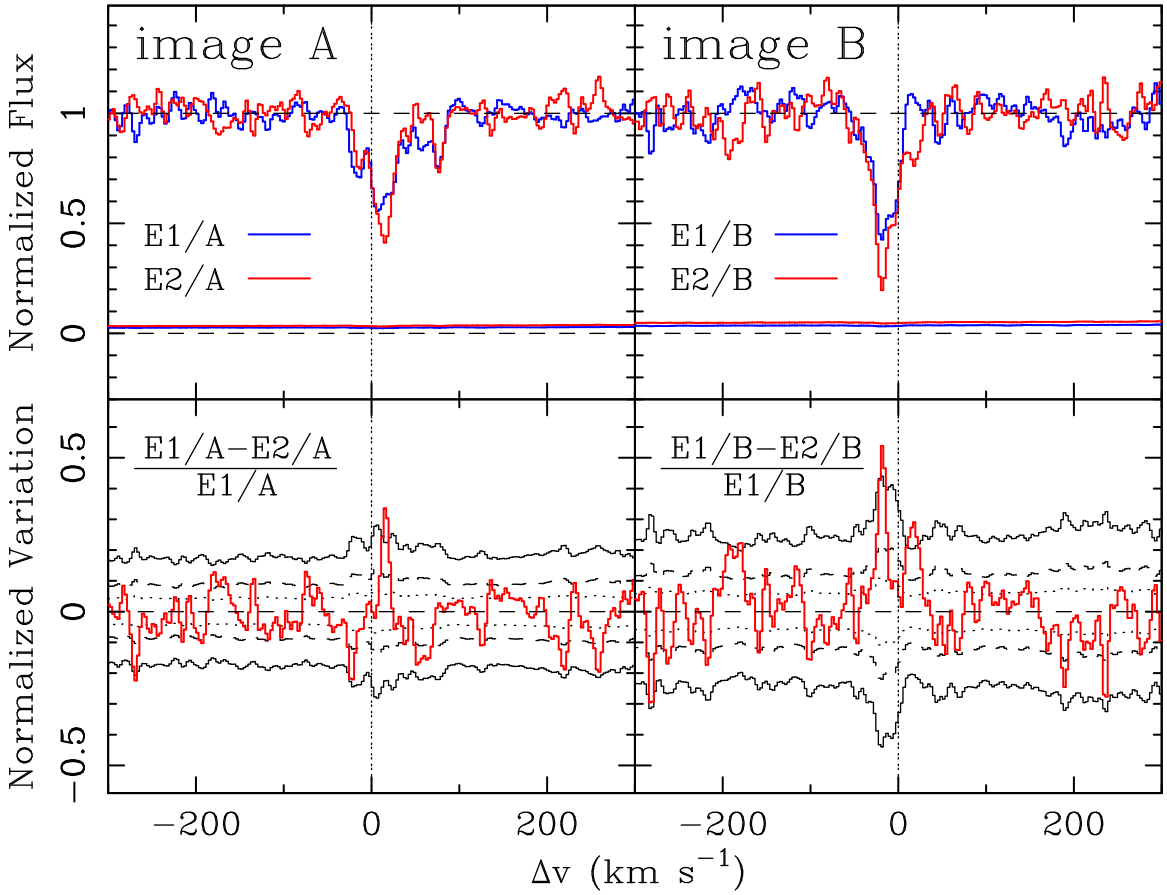

Figure 6. Comparison of normalized spectra around the Mg I NAL detected at $z_{\rm abs} = 0.8716$ in spectra of images A (upper left) and B (upper right) in epochs E1 (blue) and E2 (red). The histograms above the zero flux line are 1σ flux errors. Normalized flux variations between the spectra in two epochs as a function of velocity ((E1-E2)/E1; solid histogram) are shown for images A (lower left) and B (lower right) with 1, 2, and 4σ flux uncertainties (dotted, dashed, and solid curves). The horizontal axis is the offset velocity from $z_{\rm abs} = 0.8716$.

Assuming that variability of the Mg I NAL is due to gas motion across the sightlines, we can place an upper limit on the cloud's size as $d \leqslant v_{\rm trans}\,\Delta t_{\rm rest} \sim 22\,(v_{\rm trans}/200\,{\rm km\,s^{-1}})$ au, where we normalized the transverse velocity by the typical rotational velocity of intervening galaxies. This system could be an analog of low-ionized ($\log U \leqslant -7$) metal absorbers in a small sized ($\sim$10–100 au), cold ($<$100 K), and high volume density ($n_{\rm H} \sim 10^3$–10^6 cm^{-3}) pocket of gas with large molecular content that has been detected in the Milky Way (e.g., Diamond et al. 1989; Faison et al. 1998; Richter et al. 2003) as well as outside our Galaxy (e.g., Kanekar & Chengalur 2001; Jones et al. 2010; Hacker et al. 2013; Bergeron & Boissé 2017).

Another mechanism for the possible variability of the Mg I NAL is a change of ionization state. In this case, we can place constraints on the electron density as $n_e \geqslant 5800$ cm^{-3}, assuming that the decrease in the ionizing flux causes recombination from Mg^+ to Mg^0 (e.g., Hamann et al. 1997b; Narayanan et al. 2004). However, a change in ionization state is less likely because it rarely occurs in just a few years in foreground galaxies (Narayanan et al. 2004).

5.3. Multi-sightline Observation for Lensed Quasars

We performed high-resolution spectroscopic observations for a small-separation lensed quasar twice in this paper and for a large-separation lensed quasar SDSS J1029+2623 three times in Misawa et al. (2013, 2014b, 2016). The parameters we evaluated for the quasars based on the above observations are summarized in Table 4. As seen in Figure 10 of Misawa et al. (2016) and Figure 3 of this paper, the absorption profiles in the two lensed images are similar, which means that in both cases there is a significant overlap of the two cylinders of sight to the two lensed image. Thus, the corresponding absorbers are probably located at a distance smaller than the boundary distance (see Figure 13 of Misawa et al. 2016).

5.3.1. Intrinsic NALs in SDSS J1029+2623

As for the NAL clustering at $z_{\rm abs} \sim z_{\rm em}$ in the spectra of SDSS J1029+2623 (we called it a Proximity Absorption Line, or PAL, system in Misawa et al. 2016), we discovered that all the troughs in the PAL varied in concert, which suggests that the observed variability was not due to gas motion. Assuming the variability is due to a change of ionization, Misawa et al. (2016) placed an upper limit on its distance from the source of $r < 620$ pc by interpreting the variability timescale to be the recombination time. This distance is consistent with those evaluated for other intrinsic NAL systems in quasars that are not lensed, a few hundred parsecs to several kiloparsecs (e.g., Hamann et al. 2001; Narayanan et al. 2004; Arav et al. 2013; Borguet et al. 2013). At such a large distance, the BELR can be a background flux source that contributes along with the continuum source. Indeed, the residual flux at the bottom of the PAL is almost zero on the C IV emission line in the spectra. The boundary distance, assuming that both the continuum

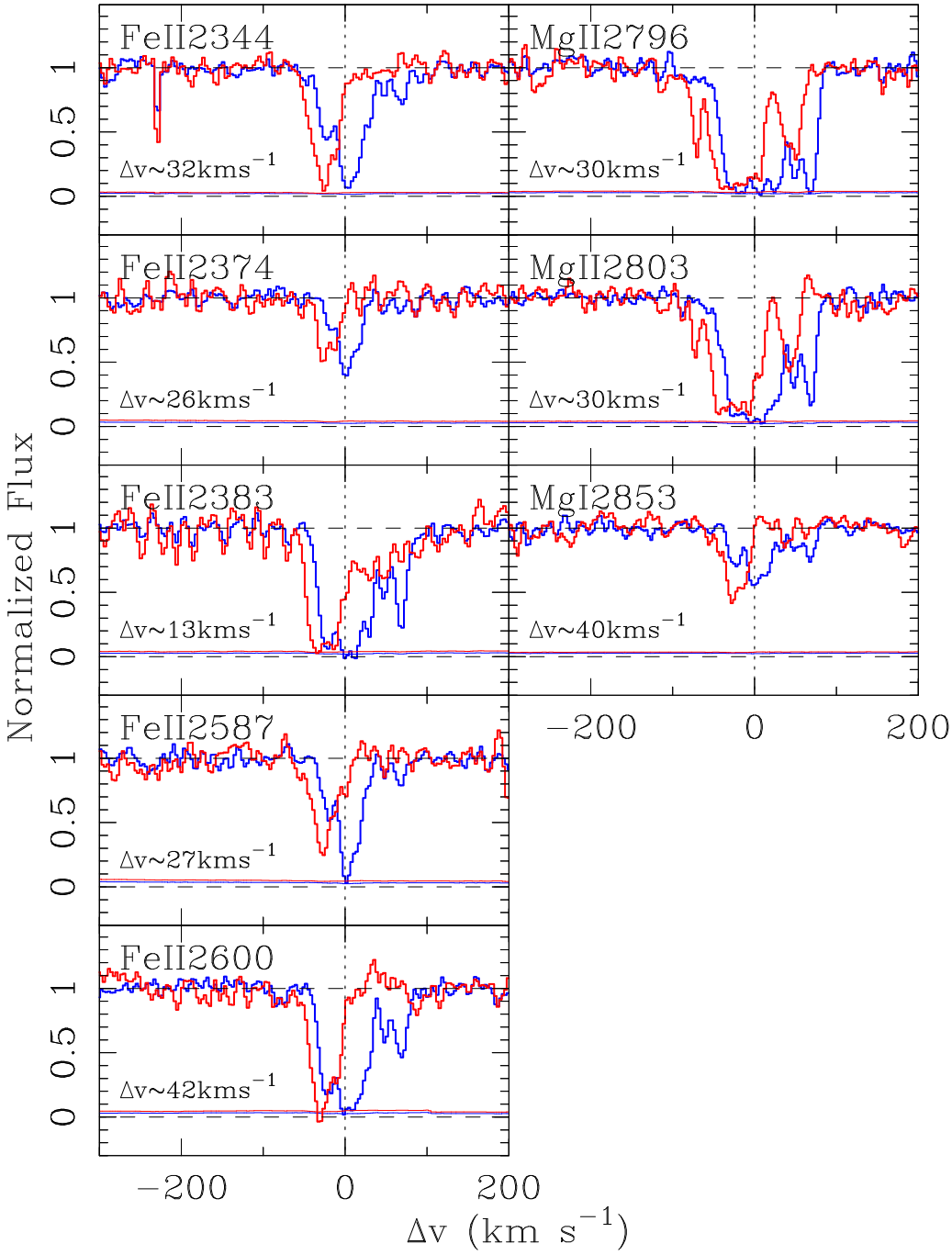

Figure 7. Comparison of normalized spectra around detected NALs of the Mg II system at $z_{\rm abs} \sim 0.8716$ in spectra of the images A (blue) and B (red) in epoch E1. The horizontal axis is the offset velocity from the flux-weighted line center of Mg II in image A ($z_{\rm abs} = 0.8716$), and the vertical axis is the normalized flux. The histograms above the zero flux line are 1σ flux errors. The numbers at the lower left corner of each panel denote the offset velocity of the NALs in image A from that in image B.

source and the BELR are background sources, is $r_{\rm b} \sim 1.2$ kpc (Misawa et al. 2016). Thus, the NAL absorbers are viewed through distinct sightlines in large-separation lensed quasars with $\theta \geqslant 10''$ because their distance from the flux source is large enough (i.e., comparable to the boundary distance).

Small-separation lensed quasars with $\theta \sim 1''$ may still provide views through distinct sightlines of NALs with very large offset velocities that are located far from the corresponding BELs in quasar spectra (i.e., only the continuum source is the background source).

5.3.2. BAL in SDSS J1001+5027

In contrast, BAL absorbers are usually located at a very small radial distance of the order of a parsec or much less (e.g., Capellupo et al. 2011, 2013). Assuming that the variability we have observed in the C IV BAL of SDSS J1001+5027 is due to a gas motion, we placed an upper limit on the absorber's distance as $r \leqslant 0.06$–0.5 pc. At such a small distance, the BAL absorbers could coexist with the BELR (Krongold et al. 2017, see also Eracleous et al. 2003). Even if only the continuum source is the background source, the corresponding boundary

Table 4
Comparison of Two Lensed Quasars

	SDSS J1029 +2623	References	SDSS J1001 +5027	References
z_{em}[a]	2.197	1	1.841	10
z_l[b]	0.58	2	0.415	11
θ (arcsec)[c]	22.5	1	2.86	10
θ' (arcsec)[d]	14.6	3	1.37	12
μ_A[e]	10.4	4	1.99	10, 12
Δt_{obs} (days)[f]	744	5	119	13
$\log L_{bol}$ (erg s^{-1})[g]	45.87	6, 7	46.93	7, 12
L_{bol}/L_{Edd}[h]	0.11	6	0.15	12
$\log M_{BH}/M_\odot$[i]	8.72	6, 7	9.66	7, 12
R_{BELR} (pc)[j]	0.09	6, 7, 8	0.37	7, 8, 12
R_{cont} (pc)[k]	2.54×10^{-4}	6, 7, 9	2.16×10^{-3}	7, 9, 12
v_{ej} (km s^{-1})[l]	0–1600	6	2500–9500	12
FWHM (km s^{-1})[m]	1600	6	7000	12
Absorption Profile[n]	NAL	6	BAL	12
Covering factor	$C_f < 1$	6	$C_f < 1$	12
Line locking	Yes	6	No	12
r_b(BELR) (kpc)[o]	1.2	3	55.6	12
r_b(cont) (pc)[p]	3.5	3	325	12

Notes.
[a] Quasar emission redshift.
[b] Redshift of lensing galaxy.
[c] Observed separation angle.
[d] Separation angle seen from the source.
[e] Magnification factor of the brightest image.
[f] Time delay between images A and B.
[g] Bolometric luminosity.
[h] Eddington Ratio.
[i] Black hole mass.
[j] Size of C IV broad emission line region.
[k] Size of the continuum source.
[l] Ejection velocity of outflowing wind.
[m] FWHM of associated absorption system.
[n] Category of absorption profile (BAL or NAL).
[o] Boundary distance considering BELR.
[p] Boundary distance considering only the continuum source.
References. (1) Inada et al. (2006); (2) Oguri et al. (2008); (3) Misawa et al. (2016); (4) Oguri et al. (2013); (5) Fohlmeister et al. (2013); (6) Misawa et al. (2013); (7) Shen et al. (2011); (8) McLure & Dunlop (2004); (9) Misawa et al. (2005); (10) Oguri et al. (2005); (11) Inada et al. (2012); (12) this paper; (13) Rathna Kumar et al. (2013).

distance is much larger than the absorber's distance (see Table 4). Thus, a multi-sightline observation is almost impossible for BAL absorbers in the vicinity of the BELR. However, large-separation lensed quasars may allow us to perform multi-sightline observation even for BAL absorbers if the absorbers are located far from the BELR and if the BAL troughs do not overlap with the BEL profiles.

6. Summary

Using the Subaru telescope, we performed high-resolution spectroscopy of the two images of the small-separation lensed quasar SDSS J1001+5027 ($\theta = 2\farcs86$) twice in a time interval of about one year to see whether the broad C IV absorption lines are variable or not. We discuss the constraints on the radial distance and physical conditions of the absorber and compare them to those obtained for the large-separation lensed quasar SDSS J1029+2623 ($\theta = 22\farcs5$). We also search for variability and compare profiles between the sightlines for NAL absorbers seen in our spectra. Our main findings are as follows:

1. We discovered variability in the C IV BALs in both lensed images. The observed variations are probably caused by gas motion around the background source (i.e., the continuum source) because the absorption components in the BAL profile do not vary in concert. We infer a rotational velocity of the absorber of $v_{rot} \geqslant 18{,}000$ km s^{-1}, and a radial distance from the center of $r \leqslant 0.06$ pc, assuming Keplerian motion.
2. Because BAL absorbers are believed to be located very close to the flux source (at a distance of the order of parsecs or less, much smaller than the boundary distance), the sightlines of the images of small-separation lensed quasars, such as SDSS J1001+5027, are not distinct. Nonetheless, the sightlines to NAL absorbers that are several kiloparsec away from the quasar are distinct (as in SDSS J1029+2623 Misawa et al. 2013, 2014b, 2016).
3. In addition to the C IV BAL system, we detected six NAL systems at $z_{abs} = 0.4147$–1.7536, of which only the Mg II system at $z_{abs} = 0.8716$ shows possible time variability in its Mg I profile and a $\sim$30 km s^{-1} velocity shear between the sightlines whose physical separation is $\sim$ 7 kpc. This is probably due to motion of the absorbing gas located in an intervening galaxy.

For further investigations of the outflow's geometrical and physical conditions through multi-sightline observations, we should mainly target intrinsic NAL absorbers with a large offset velocity from quasar redshift (i.e., their distance from the flux source is large) rather than BAL systems in the vicinity of the source. As for BALs, we can use lensed quasar spectra taken at a single epoch to examine their variability, exploiting the time delay between the lensed images.

We would like to thank the anonymous referee for extensive comments, that helped improve the paper. We would also like to thank Ken Ohsuga and Mariko Nomura for their valuable comments as well as Christopher Churchill for providing us with the MINFIT and SEARCH software packages. The research was supported by the Japan Society for the Promotion of Science through Grant-in-Aid for Scientific Research 15K05020 and partially supported by a MEXT Grant-in-Aid for Scientific Research on Innovative Areas (No. 15H05894). J.C.C. and M.E. were supported by National Science Foundation grant AST-1312686.

Facility: Subaru(HDS).
Software: IRAF, astropy (Astropy Collaboration et al. 2013).

ORCID iDs

Toru Misawa https://orcid.org/0000-0002-5464-9943
Naohisa Inada https://orcid.org/0000-0002-7534-4081
Masamune Oguri https://orcid.org/0000-0003-3484-399X
Jane C. Charlton https://orcid.org/0000-0003-4877-9116
Michael Eracleous https://orcid.org/0000-0002-3719-940X

References

Aghamousa, A., & Shafieloo, A. 2017, ApJ, 834, 31
Arav, N., Becker, R. H., Laurent-Muehleisen, S. A., et al. 1999, ApJ, 524, 566
Arav, N., Borguet, B., Chamberlain, C., Edmonds, D., & Danforth, C. 2013, MNRAS, 436, 3286
Arav, N., Edmonds, D., Borguet, B., et al. 2012, A&A, 544, A33
Astropy Collaboration, Robitaille, T. P., Tollerud, E. J., et al. 2013, A&A, 558, A33
Barlow, T. A., & Sargent, W. L. W. 1997, AJ, 113, 136
Benn, C. R., Carballo, R., Holt, J., et al. 2005, MNRAS, 360, 1455
Bergeron, J., & Boissé, P. 2017, A&A, 604, A37
Blandford, R. D., & Parne, D. G. 1982, MNRAS, 199, 883
Bordoloi, R., Tumlinson, J., Werk, J. K., et al. 2014, ApJ, 796, 136
Borguet, B. C. J., Arav, N., Edmonds, D., Chamberlain, C., & Benn, C. 2013, ApJ, 762, 49
Bowler, R. A. A., Hewett, P. C., Allen, J. T., & Ferland, G. J. 2014, MNRAS, 445, 359
Brotherton, M. S., & Wills, B. J. 1994, ApJ, 430, 495
Capellupo, D. M., Hamann, F., Shields, J. C., Halpern, J. P., & Barlow, T. A. 2013, MNRAS, 429, 1872
Capellupo, D. M., Hamann, F., Shields, J. C., Rodríguez Hidalgo, P., & Barlow, T. A. 2011, MNRAS, 413, 908
Chen, H.-W., Lanzetta, K. M., & Webb, J. K. 2001, ApJ, 556, 158
Churchill, C. W. 1997, PhD thesis, Univ. California
Churchill, C. W., Trujillo-Gomez, S., Nielsen, N. M., & Kacprzak, G. G. 2013, ApJ, 779, 87
Churchill, C. W., Vogt, S. S., & Charlton, J. C. 2003, AJ, 125, 98
Dahle, H., Gladders, M. D., Sharon, K., et al. 2013, ApJ, 773, 146
de Kool, M., Arav, N., Becker, R. H., et al. 2001, ApJ, 548, 609
Diamond, P. J., Goss, W. M., Romney, J. D., et al. 1989, ApJ, 347, 302
Elvis, M. 2000, ApJ, 545, 63
Emmering, R. T., Bladford, R. D., & Shlosman, I. 1992, ApJ, 385, 460
Eracleous, M., Halpern, J. P., & Charlton, J. C. 2003, ApJ, 582, 633
Everett, J. E. 2005, ApJ, 631, 689
Faison, M. D., Goss, W. M., Diamond, P. J., & Taylor, G. B. 1998, AJ, 116, 2916
Filiz Ak, N., Brandt, W. N., Hall, P. B., et al. 2013, ApJ, 777, 168
Fohlmeister, J., Kochanek, C. S., Falco, E. E., et al. 2013, ApJ, 764, 186
Gabel, J. R., Arav, N., & Kim, T.-S. 2006, ApJ, 646, 742
Gallagher, S. C., Brandt, W. N., Chartas, G., & Garmire, G. P. 2002, ApJ, 567, 37
Ganguly, R., Bond, N. A., Charlton, J. C., et al. 2001, ApJ, 549, 133
Ganguly, R., Eracleous, M., Charlton, J. C., & Churchill, C. W. 1999, AJ, 117, 2594
Gibson, R. R., Brandt, W. N., Schneider, D. P., & Gallagher, S. C. 2008, ApJ, 675, 985
Green, P. J. 2006, ApJ, 644, 733
Guerras, E., Mediavilla, E., Jimenez-Vicente, J., et al. 2013, ApJ, 764, 160
Hacker, T. L., Brunner, R. J., Lundgren, B. F., & York, D. G. 2013, MNRAS, 434, 163
Hamann, F., Barlow, T. A., Beaver, E. A., et al. 1995, ApJ, 443, 606
Hamann, F., Barlow, T. A., & Junkkarinen, V. 1997a, ApJ, 478, 87
Hamann, F., Barlow, T. A., Junkkarinen, V., & Burbidge, E. M. 1997b, ApJ, 478, 80
Hamann, F., Chartas, G., McGraw, S., et al. 2013, MNRAS, 435, 133
Hamann, F., Kanekar, N., Prochaska, J. X., et al. 2011, MNRAS, 410, 1957
Hamann, F., Kaplan, K. F., Rodríguez Hidalgo, P., Prochaska, J. X., & Herbert-Fort, S. 2008, MNRAS, 391, L39
Hamann, F. W., Barlow, T. A., Chaffee, F. C., Foltz, C. B., & Weymann, R. J. 2001, ApJ, 550, 142
Horiuchi, T., Misawa, T., Morokuma, T., et al. 2016, PASJ, 68, 48
Inada, N., Oguri, M., Morokuma, T., et al. 2006, ApJL, 653, L97
Inada, N., Oguri, M., Pindor, B., et al. 2003, Natur, 426, 810
Inada, N., Oguri, M., Shin, M.-S., et al. 2012, AJ, 143, 119
Jones, T. M., Misawa, T., Charlton, J. C., Mshar, A. C., & Ferland, G. J. 2010, ApJ, 715, 1497
Kacprzak, G. G., Churchill, C. W., & Nielsen, N. M. 2012, ApJL, 760, L7
Kanekar, N., & Chengalur, J. N. 2001, MNRAS, 325, 631
Konigl, A., & Kartje, J. F. 1994, ApJ, 434, 446
Koyamada, S., Misawa, T., Inada, N., et al. 2017, ApJ, 851, 88
Krongold, Y., Binette, L., Bohlin, R., et al. 2017, MNRAS, 468, 3607
Krongold, Y., Nicastro, F., Elvis, M., et al. 2007, ApJ, 659, 1022
Marziani, P., Sulentic, J. W., Dultzin-Hacyan, D., Calvani, M., & Moles, M. 1996, ApJS, 104, 37
McLure, R. J., & Dunlop, J. S. 2004, MNRAS, 352, 1390
Misawa, T., Charlton, J. C., Eracleous, M., et al. 2007a, ApJS, 171, 1
Misawa, T., Charlton, J. C., & Eracleous, M. 2014a, ApJ, 792, 77
Misawa, T., Eracleous, M., Charlton, J. C., & Kashikawa, N. 2007b, ApJ, 660, 152
Misawa, T., Eracleous, M., Charlton, J. C., & Tajitsu, A. 2005, ApJ, 629, 115
Misawa, T., Inada, N., Oguri, M., et al. 2014b, ApJL, 794, L20
Misawa, T., Inada, N., Ohsuga, K., et al. 2013, AJ, 145, 48
Misawa, T., Saez, C., Charlton, J. C., et al. 2016, ApJ, 825, 25
Moe, M., Arav, N., Bautista, M. A., & Korista, K. T. 2009, ApJ, 706, 525
Moravec, E. A., Hamann, F., Capellupo, D. M., et al. 2017, MNRAS, 468, 4539
Morgan, C. W., Kochanek, C. S., Morgan, N. D., & Falco, E. E. 2010, ApJ, 712, 1129
Narayanan, D., Hamann, F., Barlow, T., et al. 2004, ApJ, 601, 715
Nestor, D., Hamann, F., & Rodríguez Hidalgo, P. 2008, MNRAS, 386, 2055
Netzer, H., Lira, P., Trakhtenbrot, B., Shemmer, O., & Cury, I. 2007, ApJ, 671, 1256
Oguri, M., Inada, N., Hennawi, J. F., et al. 2005, ApJ, 622, 106
Oguri, M., Ofek, E. O., Inada, N., et al. 2008, ApJL, 676, L1
Oguri, M., Schrabback, T., Jullo, E., et al. 2013, MNRAS, 429, 482
Rathna Kumar, S., Tewes, M., Stalin, C. S., et al. 2013, A&A, 557, A44
Richter, P., Sembach, K. R., & Howk, J. C. 2003, A&A, 405, 1013
Rodríguez Hidalgo, P., Eracleous, M., Charlton, J., et al. 2013, ApJ, 775, 14
Rusu, C. E., Oguri, M., Minowa, Y., et al. 2016, MNRAS, 458, 2
Scannapieco, E., & Oh, S. P. 2004, ApJ, 608, 62
Shakura, N. I., & Sunyaev, R. A. 1973, A&A, 24, 337
Shen, S., Madau, P., Aguirre, A., et al. 2012, ApJ, 760, 50
Shen, Y., Richards, G. T., Strauss, M. A., et al. 2011, ApJS, 194, 45
Springel, V., Di Matteo, T., & Hernquist, L. 2005, ApJL, 620, L79
Srianand, R., Petitjean, P., Ledoux, C., & Hazard, C. 2002, MNRAS, 336, 753
Stern, J., Hennawi, J. F., Prochaska, J. X., & Werk, J. K. 2016, ApJ, 830, 87
Sulentic, J. W., del Olmo, A., Marziani, P., et al. 2017, A&A, 608, 122
Trevese, D., Saturni, F. G., Vagnetti, F., et al. 2013, A&A, 557, A91
Turner, M. L., Schaye, J., Steidel, C. C., Rudie, G. C., & Strom, A. L. 2014, MNRAS, 445, 794
Turnshek, D. A., Chae, K.-H., Rao, S. M., et al. 2001, in ASP Conf. Ser. 237, Gravitational Lensing: Recent Progress and Future Goals, ed. T. G. Brainerd & C. S. Kochanek (San Francisco, CA: ASP), 105
Vestergaard, M. 2003, ApJ, 599, 116
Vivek, M., Srianand, R., & Gupta, N. 2016, MNRAS, 455, 136
Vivek, M., Srianand, R., Petitjean, P., et al. 2012, MNRAS, 423, 2879
Vivek, M., Srianand, R., Petitjean, P., et al. 2014, MNRAS, 440, 799
Wampler, E. J., Chugai, N. N., & Petitjean, P. 1995, ApJ, 443, 586
Weymann, R. J., Morris, S. L., Foltz, C. B., & Hewett, P. C. 1991, ApJ, 373, 23
Weymann, R. J., Williams, R. E., Peterson, B. M., & Turnshek, D. A. 1979, ApJ, 234, 33
Wise, J. H., Eracleous, M., Charlton, J. C., & Ganguly, R. 2004, ApJ, 613, 129
York, D. G., Adelman, J., Anderson, J. E., Jr., et al. 2000, AJ, 120, 1579